Understanding pilot biodynamical feedthrough coupling in helicopter adverse roll axis instability via lateral cyclic feedback control

Georges Tod [a,*], Marilena D. Pavel [b], François Malburet [a], Julien Gomand [a],
Pierre-Jean Barre [a]

[a] *Arts et Métiers ParisTech, CNRS LSIS, 13617 Aix-en-Provence, France*
[b] *Delft University of Technology, 2629HS Delft, The Netherlands*

The paper reassesses the mechanism of biodynamical feedthrough coupling to helicopter body motion in lateral-roll helicopter tasks. An analytical bio-aeroelastic pilot–vehicle model is first developed and tested for various pilot's neuromuscular adaptions in the lateral/roll axis helicopter tasks. The results demonstrate that pilot can destabilize the low-frequency regressing lead-lag rotor mode; however he/she is destabilizing also the high-frequency advancing lag rotor mode. The mechanism of pilot destabilization involves three vicious energy circles, i.e. lateral-roll, flap-roll and flap-lag motions, in a very similar manner as in the air resonance phenomenon. For both modes, the destabilization is very sensitive to an increase of the steady state rotor coning angle that increases the energy transfers from flap to lag motion through Coriolis forces. The analytical linear time-invariant model developed in this paper can be also used to investigate designs proneness to lateral/roll aeroelastic rotorcraft–pilot couplings.

1. Introduction

Biodynamic feedthrough (BDFT) refers to a phenomenon where vehicle accelerations cause involuntary pilot limb motions which, when coupled to a control device, can result in unintentional pilot control inputs. BDFT effects in helicopters have been identified since the beginning of helicopter operations [1–4]. In particular, pilot interaction with helicopter airframe structural modes has been of concern for BDFT in rotorcraft [5]. This interaction involves passive pilot participation, with low frequency airframe structural modes, frequently via flight control system (FCS) interaction, which induces oscillations at a particular airframe structural mode. Commonly referred to as pilot augmented or assisted oscillations (PAOs) – or more generally aeroelastic Rotorcraft–Pilot-Couplings (RPCs) – these phenomena need efficient engineering solutions as they can result in catastrophic accidents [6,7].

Aeroelastic RPC/PAO existence is often associated with induced oscillations at a particular structural mode. Fig. 1 presents the pilot in the loop subsystems that interact during PAO via his/her cyclic lever. The pilot, through the muscles in the neuromuscular system, controls the aircraft response to disturbances and the task to be flown. In modern aircraft, the pilot inceptor is not connected to the vehicle directly but through an integrated FCS. Sometimes the aircraft vibratory environment affects the pilot's biodynamic response and generates involuntary inputs. The coupled rotor–fuselage aeroelastic motions are fed back to the pilot.

For example, experiences in soft-inplane hinge-or-bearingless (i.e. when natural frequency of the rotor blade lead-lag (in-plane) motion ω_δ is smaller than rotor angular velocity Ω, $\omega_\delta < \Omega$) rotor helicopters reveal that, when the helicopter is enhanced with FCS, the weakly damped lead-lag motion characterizing these special kind of rotors can become unstable through pilot control inputs. This was the case of EC135 helicopter instability reported in [8]: in the basic helicopter operation condition, the air resonance mode instability was not an issue for the pilots operating the EC135. Air resonance mode resembles the interaction of the low-frequency blade lead-lag mode as seen in the nonrotating reference frame – the so-called regressing lag mode – with the low frequency flap-roll mode. The air resonance instability in EC135 manifested as a body roll oscillation which was existent but it was below the pilot perception level. However, when the helicopter was enhanced with an Attitude command/Attitude Hold (ACAH) control system for flying attitude command or flight path following tasks, it appeared that, increasing too much the roll rate feedback gain, the air resonance mode was driven unstable. This time the body

x	airframe lateral translation	m
a_x	airframe lateral acceleration	m/s^2
z	airframe vertical translation	m
α_y	airframe roll angle	rad
$\beta_i, \delta_i, \theta_i$	individual blade flap, lag and pitch angles	rad
$\beta_0, \beta_{1c}, \beta_{1s}$	collective and cyclic blades flap angles	rad
$\delta_0, \delta_{1c}, \delta_{1s}$	collective and cyclic blades lag angles	rad
$\theta_0, \theta_{1c}, \theta_{1s}$	collective and cyclic blades pitch angles	rad
b	main rotor number of blades	
R	rotor radius	m
e	blade root eccentricity	m
γ	lock number	
Ω	main rotor angular velocity	rad/s
β_{0ss}	steady-state coning angle	rad
m_s	individual blade static moment at blade root	m kg
I_{bl}	individual blade inertia at blade root	m^2 kg
M_{bl}	individual blade mass	kg
k_δ	individual blade equivalent angular lag damper stiffness	N m/rad
c_δ	individual blade equivalent angular lag damper damping	N m s/rad
M_f	helicopter mass	kg
I_{yy}	airframe roll inertia around its center of mass	m^2 kg
h	rotor head height from airframe center of mass	m
G	gearing ratio	
ω	pilot biodynamics resonant frequency	rad/s
k	pilot biodynamics gain	
ζ	pilot biodynamics damping	1/s

Abbreviations

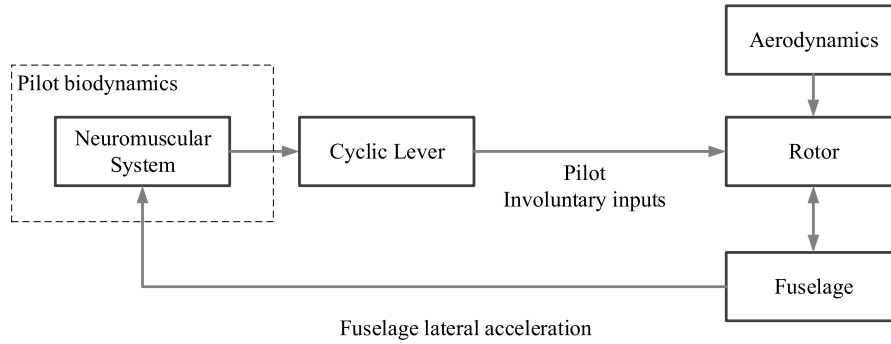|	
PIO	Pilot Induced Oscillations
PAO	Pilot Assisted Oscillations
RPC	Rotorcraft Pilot Coupling
BDFT	Biodynamic Feedthrough
dof(s)	degree(s) of freedom
FPM	forcing phasing matrices

Fig. 1. Main subsystems interactions in helicopter BDFT phenomena related to cyclic control.

roll oscillation was perceived by the pilot as an oscillatory ringing in the helicopter roll response at a frequency of about 1.8 Hz. It was demonstrated that in this case the EC135 helicopter was PAO prone in the lateral axis when applying the bandwidth criterion as described in the ADS-33 handling qualities standard [9]. In order to damp the air resonance mode when rate feedback was used, [8] developed an air resonance controller needed to be implemented in the main FCS which effectively damped the coupled body–roll air resonance mode.

Other examples of BDFT in helicopters relate to the collective bounce (vertical bounce) and the roll axis instability. Collective bounce is the consequence of adverse interaction of the pilot with the vertical motion of the helicopter via the collective control [1, 4,10,11,25]. Roll axis instability is caused by involuntary motions of the pilot's arm in the cyclic control which couple to the lag/roll dynamics of the helicopter. In fixed-wing aircraft, the source of adverse pilot–roll dynamics coupling has been often identified either in the flexibility of the vehicle (e.g. low frequency skew-symmetric wing bending that interacts with rigid body roll dynamics to generate sufficient phase delay in roll response) or other sources of delay (e.g. input processing by a digital flight control system, insufficient bandwidth, saturation of control system actuators). In helicopters, roll axis instability is mainly attributed to the regressing lead-lag mode as this mode eigenfrequency is close to pilot biodynamics [12]. The literature of specialty explains mainly the pure mechanism through which the flap-lag rotor motions can couple

to lateral/roll via FCS feedback, however without the involvement of pilot biodynamics [13,14]. When involving pilot biodynamics, it is recognized that "*predictions suggest that the roll/lateral PAO phenomena are more likely to occur on helicopters with soft in-plane rotors that have lightly damped in-plane rotor modes, more sensitive to time delay than gearing ratio with respect to the lateral cyclic control, more dangerous when the flight speed increases and more likely to occur with pilots that are characterized by a natural frequency of the biodynamic poles that is close to the lightly damped in-plane rotor mode*" [12]. The goal of the present paper is to give a thorough understanding of the mechanism through which the pilot can destabilize the air resonance mode and induce roll axis instability via cyclic control stick feedback. It will be demonstrated that not only the low-frequency regressing lead-lag mode is the mode responsible for coupling to pilot biodynamics but also that the high-frequency advancing lead-lag mode can induce translational and rotational airframe motions manifested at low frequency as vertical and lateral rigid body vibrations with strong degradation in ride qualities.

2. Mathematical modeling for roll helicopter–pilot coupling

2.1. Helicopter aeromechanical lateral-roll dynamics model

In the following, an air resonance model in hover is briefly described. First, a non-linear aeromechanical model is developed in the rotating system of reference using Lagrange equa-
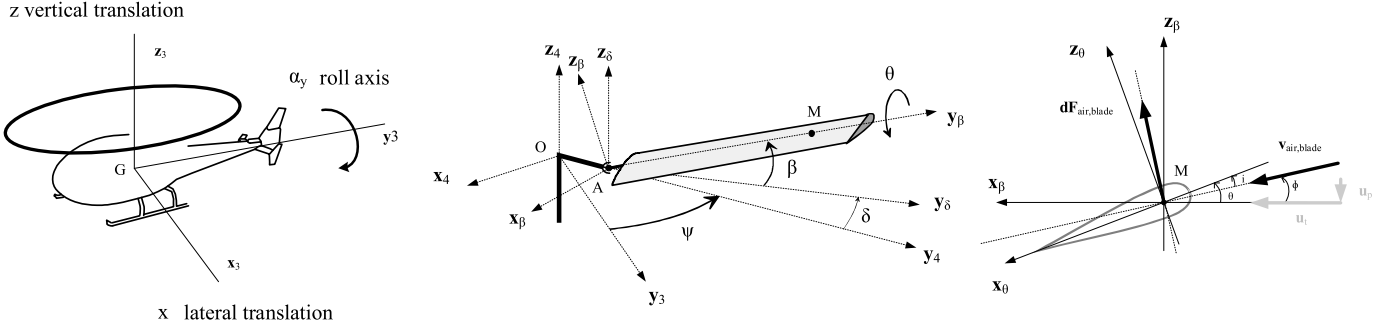
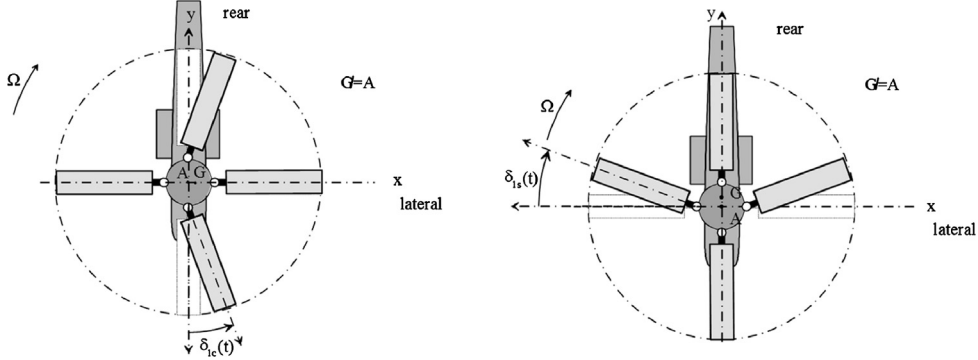**Fig. 2.** Axis definitions of the rotorcraft model.

Fig. 3. Rotor advancing and regressing lag modes seen as lateral and longitudinal center of gravity G shifts [15].

tions. For a 4-bladed rotor the model accounts 11-dof $\mathbf{q} = [x, z, \alpha_y, \beta_1, \beta_2, \beta_3, \beta_4, \delta_1, \delta_2, \delta_3, \delta_4]^T$ for the coupled fuselage-rotor motion that includes 3-dof for the fuselage motion (fuselage lateral translation x, fuselage vertical translations z and fuselage roll α_y), 4-dof corresponding to each blade flapping motion $\beta_1, \beta_2, \beta_3, \beta_4$ and 4-dof corresponding to each blade lead-lag motion $\delta_1, \delta_2, \delta_3, \delta_4$, see Fig. 2. The rotor–airframe modeling accuracy is aligned to the minimum level needed to investigate air resonance phenomena (see for example [15,16]). The model includes quasi-steady aerodynamics, which is sufficient when investigating low frequency phenomena [17]. No inflow velocity is considered since it is reported in [18] that the inflow is generally faster than the dynamics of interest and can be reasonably approximated by replacing the Lock number with the reduced Lock number: usually between 60 to 70% of Lock number [18].

The peculiarity of rotorcraft w.r.t. fixed-wing aircraft is that low-frequency pilot inputs can generate high-frequency blade excitations. This is because, in the case of rotorcraft control, moments are transmitted indirectly from the pilot stick to the rotor through the swashplate mechanism. Pilot cyclic inputs are applied at 1/rev-frequency through this swashplate mechanism and can generate high-frequency rotor blade excitations, in the form of flap and lag motion, which can be transformed back to the fixed airframe system, where a new 1/rev-frequency shift occurs to a lower and higher frequency.

For studying the helicopter-rotor coupled motion, the blades motion as given by flapping and lead-lag motions should not be considered in the rotor rotating frame of reference, but rather in the non-rotating frame of reference fixed to the body. It is therefore essential to first transform the blade flapping/lead-lag equations to the body frame. This may be done by applying the so-called "Multiblade Coordinate Transformation (MCT)" or "Coleman transformation". This transformation accounts for the cumulative effect of the motion of all rotor blades as seen by the body. The transformation makes use of the multicyclic symmetry of the rotor (all blades are identical) to cancel periodic coefficients and leads

to simplifications and elimination of periodic coefficients in the flapping/lead-lag equations of motion in the non-rotating frame. When the MCT transformation is applied, it appears that in general, the transient blade motion splits into three levels: a relatively low-frequency 'regressing' mode, an intermediate 'coning' mode, a high frequency 'advancing mode' (see Fig. 3). For a rotor with an even number of blades the differential (reactionless) mode is introduced, this is because the MCT transformation must include the same number of modes as the number of blades (4 blades for the helicopter considered in this paper). However, the differential mode is a highly damped oscillation with the same frequency and damping as the rotating flap response and is often neglected in body-rotor motion analysis, this is because it does not respond to the conventional cyclic control inputs [19]. Therefore in this paper the differential mode was neglected as being of little interest. Neglecting the differential flapping and differential lagging modes, the 11-dof model was reduced to a 9-dof model.

In order to comprehend this frequency transformation behavior of multi-bladed rotor systems, the concept of rotor modes is helpful:

1) Collective rotor mode oscillations are transferred directly without frequency shift.
2) Cyclic rotor mode oscillations (so-called regressing and advancing modes) are transformed with ± 1/rev frequency shift. For blade lag motion, the regressing and advancing lag modes are equivalent with the rotor lateral and longitudinal center of gravity shift in the rotor plane, see Fig. 3.

As a result, a 9-dofs body-rotor model is obtained in the non-rotating system of reference $\mathbf{q} = [x, z, \alpha_y, \beta_0, \beta_{1c}, \beta_{1s}, \delta_0, \delta_{1c}, \delta_{1s}]^T$ corresponding to 3-dof for the fuselage motion (fuselage lateral translation x, fuselage vertical translation z and fuselage roll α_y), 3-dof for the disc-tilt motion (rotor coning β_0, regressing flap and advancing flap modes β_{1c}, β_{1s}) and 3-dof for lead-lag motion (coning lag δ_0, regressing and advancing lag modes δ_{1c}, δ_{1s}). The 9-dof
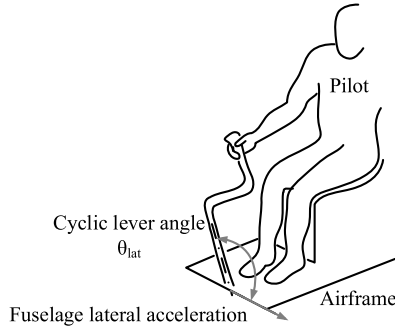
Fig. 4. Pilot seating configuration.

air resonance model is then linearized around a steady state, this is the hover condition, see eq. (1),

$$\mathbf{q_{ss}} = [0, 0, 0, \beta_{0ss}, 0, 0, 0, 0, 0]^T \tag{1}$$

The hypothesis of linearity around hover flight can be justified for example by [20], in which a helicopter dynamics linear model is developed and compared to flight tests of Sikorsky's CH-53E in hover; the results show a good agreement between the model and the tests for a range of frequencies between 1 and 10 Hz. Nonlinear models are necessary for large amplitude maneuvers [20], however since low frequency roll axis instability via cyclic control is in the range of 2 to 8 Hz [6], the blades and fuselage can be considered as rigid bodies [17]. The final expressions of the equations of motion are given in (A.1)–(A.9).

2.2. Human pilot biodynamics modeling

When a pilot is engaged in a manual control task under vehicle accelerations, see Fig. 4, these vibrations can cause involuntary limb motions leading to involuntary control inputs, i.e. biodynamic feedthrough (BDFT). It is known that pilots adapt their response and therefore their body to task instruction, workload and fatigue [4]. To account for pilot BDFT behavior, one needs to model his/her neuromuscular system adaption, i.e. his/her biodynamics. Two approaches can be identified when modeling pilot biodynamics: the first approach consists in identifying from experiments the human body response in the frequency domain due to fuselage accelerations [3]; the second approach consists in using multibody approach to capture his/her skeletal motion superposed to dynamic models of the central nervous system control [11,21,22]. The first approach usually leads to simple pilot models, easy to be coupled to vehicle models; however this approach has a limited validity as it is coupled to the experiment in which it was obtained. While a more complex pilot skeletal/muscles multibody modeling approach may help testing a large number of cabin configurations/human variability of the neuromuscular system, the simple pilot models obtained through identification experiments have the advantage of giving a global understanding of the pilot–vehicle couplings.

The BDFT modeling approach of this paper consists in representing the pilot biodynamics as a function identified in the simulator experiments performed in [3] in the SIMONA simulator at TU Delft. The expression of this second order transfer function taken from [3] is,

$$H(s) = \frac{\theta_{lat}}{a_x} \approx \frac{k.\omega^2}{\omega^2 + 2.\zeta.\omega.s + s^2} \tag{2}$$

Eq. (2), embodies the potential variation of BDFT as a function of the frequency/amplitude representing the human body neuromuscular adaption. The function can be represented as seen in Fig. 5, taken from [3]. According to the experiments at TU Delft, pilot biodynamic varies between the subjects available and the piloting tasks performed. Between different human subjects, pilots' responses are dependent on their body shapes or somatotypes, i.e. ectomorphic or mesomorphic [1]. Secondly, between the different tasks performed in [3], i.e. a position task (PT) where the pilot is minimizing the position stick, a force task (FT) where the force applied to the stick is minimized, and a relax task (RT) where the pilot relaxes his arm, the highest resonant frequency in pilot BDFT responses corresponds to the position tasks (PT). This corresponds to the maximum stiffness in the neuromuscular system and shows that it is achieved in a position task. Similar conclusions were also reported in [23], accompanied by the observation that the body 'stiffens' during urgent tracking tasks. The variability of pilot biodynamics can be therefore characterized with pilot attitudes that can be qualified as 'stiffer' in the case of stressful, high gain tracking tasks or 'relaxed' when the pilot's workload is lower.
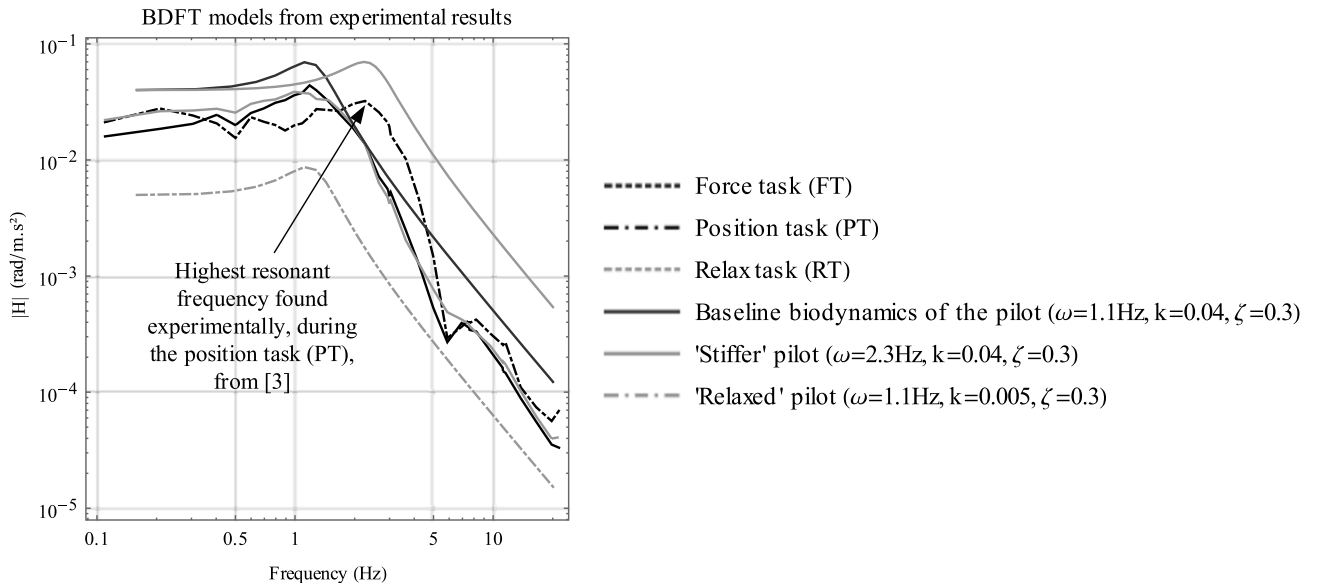
Fig. 5. Models of pilot biodynamics envelopes, adapted from [3].

Pilot biodynamics		Baseline	'Stiffer'	'Relaxed'
Resonant frequency	ω (Hz)	1.1	↗ 2.3	1.1
Gain	k	0.04	0.04	↘ 0.005
Damping	ζ (1/s)	0.3	0.3	0.3

For the biodynamic analysis in this paper, a 'Baseline' biodynamic pilot model is chosen and then varied in terms of frequency (higher frequency corresponding to a 'Stiffer' pilot) and amplitude (lower gain corresponding to a 'Relaxed' pilot), see Table 1. This allows an investigation of the pilot biodynamic shifts in terms of BDFT frequency and BDFT amplitude.

The pilot biodynamics model of eq. (2) is rewritten in its Linear Time-Invariant (LTI) formulation, see eq. (3):

$$-G\omega^2\theta_{1c} - 2G\zeta\omega\dot{\theta}_{1c} + k\omega^2\ddot{x} - G\ddot{\theta}_{1c} = 0 \qquad (3)$$

where parameter G corresponds to kinematic ratio between the maximum lateral blade pitch angle and lateral cyclic control angle, $\theta_{lat} = G\theta_{1c}$.

2.3. Pilot–vehicle coupled model

Next, the vehicle model, eqns. (A.1)–(A.9) is coupled to the pilot biodynamic model, eq. (3) and expressed in its matrix formulation as:

$$M\ddot{q} + C\dot{q} + Kq = 0 \qquad (4)$$

where $\mathbf{q} = [x, z, \alpha_y, \beta_0, \beta_{1c}, \beta_{1s}, \delta_0, \delta_{1c}, \delta_{1s}, \theta_{1c}]^T$ represents the state vector and M, C and K respectively the mass, damping and stiffness matrices. The final equations of motions in their metrical form are given in Appendix A, eqns. (A.10)–(A.13).

3. Physical insight into aeroelastic roll axis instability via cyclic control stick feedback

3.1. Pilot–vehicle modal analysis

This section examines how pilot biodynamics couples to lateral/roll helicopter dynamics. As basis for the numerical analysis, a medium weight 4-bladed helicopter, is chosen, see Table 2. This

Main rotor		
Number of blades	b	4
Radius	R (m)	7.5
Blade root eccentricity	e (m)	0.3
Lock number	γ	9
Angular velocity	Ω (rad/s)	29
Steady-state coning angle	β_{0ss} (rad)	$\pi/180$
Individual blade		
Static moment	m_s (m kg)	300
Inertia	I_{bl} (m² kg)	1500
Mass	M_{bl} (kg)	100
Equivalent angular lag damper stiffness	k_δ (N m/rad)	160000
Equivalent angular lag damper damping	c_δ (N m s/rad)	3000
Airframe		
Mass	M_f (kg)	7500
Roll inertia around center of mass	I_{yy} (kg)	10000
Rotor head height from center of mass	h (m)	2
Cyclic blade pitch/lever roll angle		
Gearing ratio	G	0.1

helicopter has a soft-inplane rotor with lightly damped in-plane rotor modes, $\omega_\delta = \sqrt{k_\delta/I_{bl}} = 1.64$ Hz ($\approx 0.35\Omega < \Omega$). This is an interesting characteristic, as soft-inplane rotors seem more prone to roll axis instability via cyclic control.

3.1.1. Helicopter modal analysis

Fig. 6 presents the pure vehicle eigenvalues (eqs. (A.1) to (A.9)), without the inclusion of pilot biodynamics characteristics. It also presents the system mode shapes normalized around the roll rate (α'_y). One can see a classical distribution of the first flap and lag modes: the advancing flap mode (8.60 Hz) and the regressing flap mode (0.67 Hz) are highly damped, while the advancing lag (6.91 Hz) and regressing lag (2.57 Hz) are lightly damped. Concerning the mode shapes, one can see that the highest contributors to the motion correspond to the regressing and advancing lag mode $\delta'_{1c,s}$ followed, in a smaller range, by regressing and advancing flapping $\beta'_{1c,s}$ (flapping motion) and lateral-roll motions (x', α'_y).

The lightly damped collective lag mode δ_0 shown in Fig. 6 is fully decoupled from other dofs and therefore it will be not influenced by pilot biodynamics. The collective flap mode β_0 which is very close to the rotor angular velocity Ω is coupled to the vertical motion z of the helicopter. Based on the modal shapes
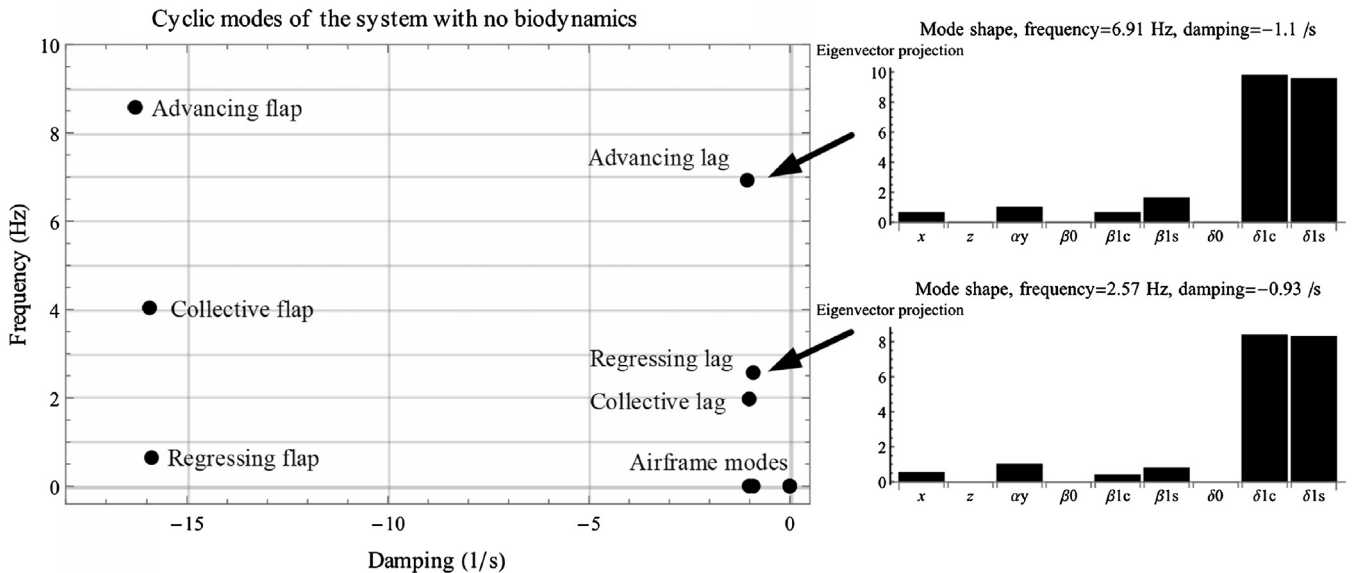
Fig. 6. Rotor flap and lead-lag eigenvalues and mode shapes without pilot biodynamics.
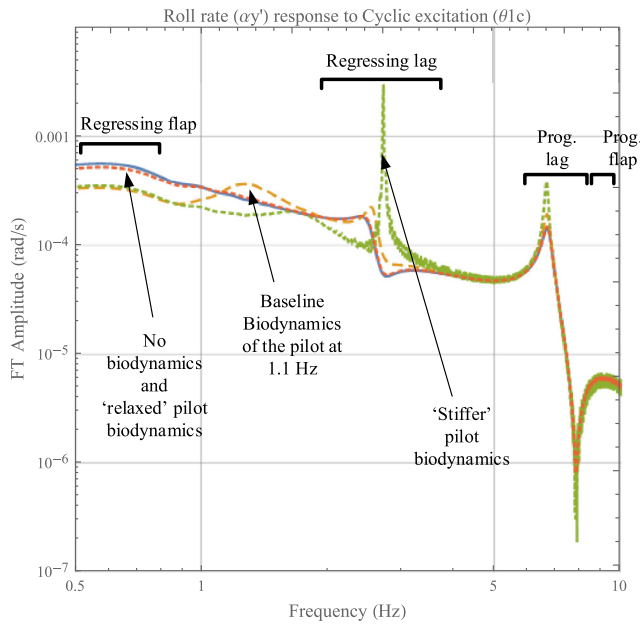
Fig. 7. Helicopter roll rate response in the frequency domain.

Fig. 8. Rotor lead-lag eigenvalues with different pilot biodynamics.

Fig. 9. Sensitivity of lag modes to pilot biodynamics resonant frequency and gain.

of Fig. 6, one can see that the airframe translational modes are close to the origin and can be considered decoupled from the rotor and pilot. These will therefore not be affected by pilot biodynamics.

3.1.2. Coupled helicopter–pilot modal analysis including pilot biodynamics

Fig. 7 depicts the helicopter roll rate response as identified by a discrete Fourier transformation for a cyclic pitch θ_{1c} sweep given between 0 and 10 Hz. Two cases are plotted, first when no pilot biodynamics is included in the model (continuous lines) and second when the baseline pilot biodynamics model is coupled to the vehicle. In both cases one can see that higher roll rate amplitude peaks can be found around both regressing and advancing lag modes, this was also found by [20].

When pilot biodynamics is involved in the motion, three changes can be seen in Fig. 7:

1) At 1.1 Hz there is an extra amplitude peak in the vehicle roll rate response caused by pilot biodynamics.
2) The shape of the roll rate response changes in the low-frequency range around regressing flap mode.
3) An increase in the vehicle roll rate response appears due to the regressing lag mode, this revealing the loss of damping around this mode.

Next, the pilot biodynamic characteristics are varied to a 'Stiffer' pilot (by increasing his resonant frequency) and to a 'Relaxed' pilot (by decreasing his gain) according to the data of Table 1. The vehicle–pilot eigenvalues are represented in Fig. 8. Looking at this figure, one can see that a stiffer pilot destabilizes the regressing lag mode. This was also concluded by [12]. However, from this figure it appears that the 'Stiffer' pilot is destabilizing not only the regressing lag mode but also the high-frequency advancing lag mode – although this mode's frequency is higher (6.91 Hz) than pilot biodynamics (1.1 Hz and 2.3 Hz). The 'Relaxed' pilot shows a better "damping" than both the 'baseline' and the 'stiffer' pilots, his damping is as the case of 'no pilot biodynamics'.
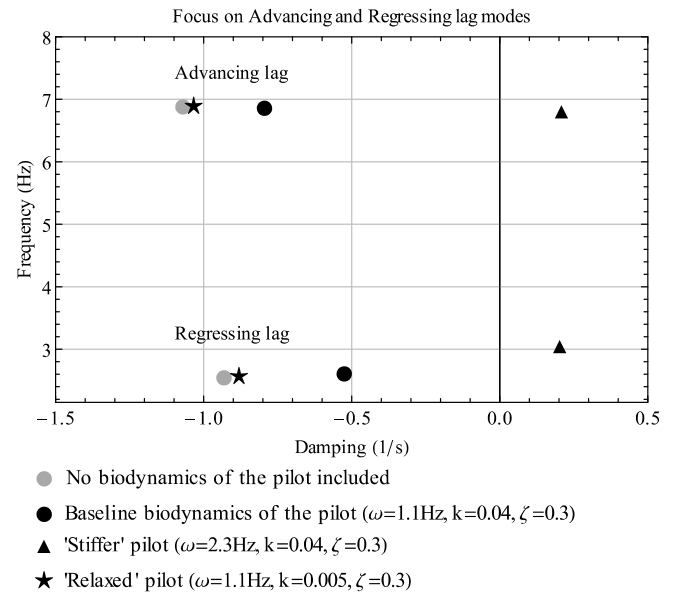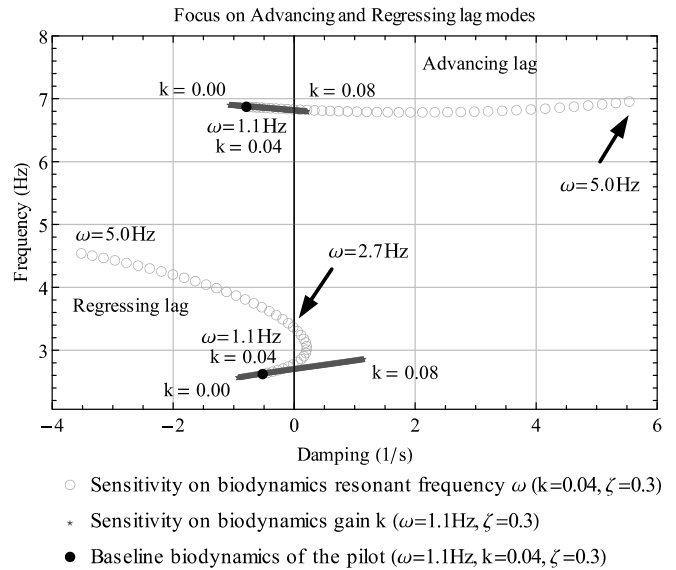
3.1.3. Sensitivity of lag modes to pilot biodynamics resonant gain and frequency

In order to understand the effect of pilot biodynamics on lag regressing and advancing modes, firstly, the pilot biodynamics gain is varied in the range of $k = 0.00$ to 0.08, keeping his resonant frequency constant. Secondly, his resonant frequency is varied between 1 and 5 Hz keeping his gain constant, see Fig. 9.

Then, both pilot gain and frequency are varied simultaneously along a range ($k = 0.02$ to 0.08) and frequency (1 to 5 Hz), see Fig. 10. One should recall the fact that these two parameters represent the adaption of the neuromuscular system to a given task or state of the pilot (stressed, relaxed) and somatotype. Looking at Fig. 9 one can see that, varying the pilot's biodynamics gain leads to a similar behavior in damping of both advancing and regressing modes, i.e. higher pilot gain leads to lower lag mode damping.

However, when both pilot biodynamics' gain and frequency are varied, the rotor lag modes react differently: while *regressing lag mode recovers its damping (2.7 Hz is the point of neutral damping for*
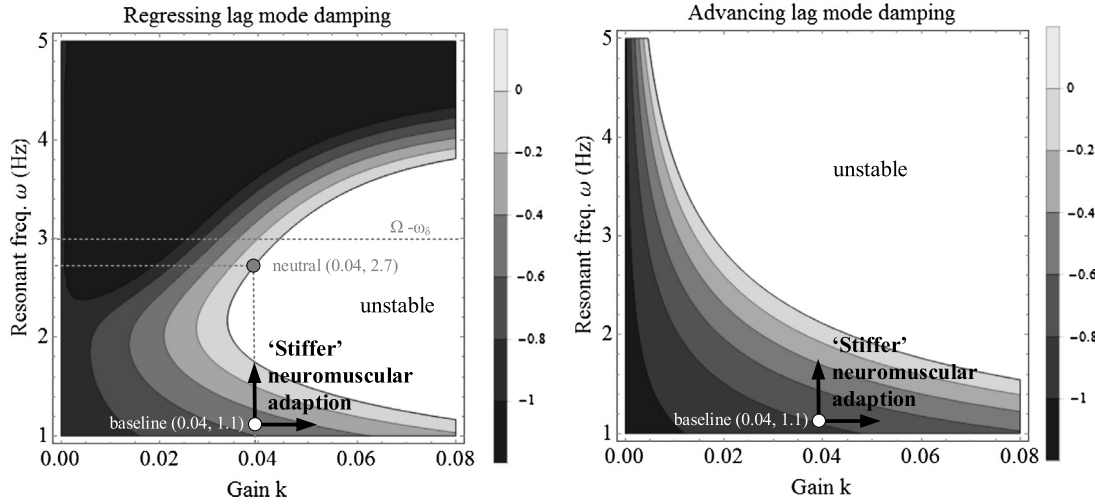
Fig. 10. Pilot biodynamics neuromuscular system adaption impact on stability of lag modes.

regressing lag), the advancing lag mode (6.91 Hz) is continuously losing is damping. More precisely, when the pilot stiffens (higher gain), the advancing lag mode becomes less damped than the regressing mode. This means that, when the pilot modifies his mindset due to a change of task or workload (for example he/she is asked to perform a high precision maneuver) he/she will tend to 'stiffen' himself/herself, adapting his/her neuromuscular system unconsciously to higher gains and frequencies, see also Fig. 5. The loss of damping of the regressing lag mode due to its proximity to the pilot biodynamics mode will be evidenced more clearly in Fig. 11 representing the Campbell diagrams of the pilot–vehicle system.

3.1.4. Sensitivity of lag modes to air density and steady state rotor coning angle

In [12], the investigation on "*the roll/lateral PAO phenomena predictions suggest they are [...] more dangerous when the flight speed increases*". The increase of the steady state rotor coning angle β_{0ss} is a way of studying the dynamic behavior of the system for higher load factors, which is an artificial way of experimenting what would happen the helicopter forward velocity increases. However, one should keep in mind the aerodynamic model used in this paper is especially valid around hover or low advancing speeds. More relevant models should be used in the future to investigate the phenomenon at high advancing speeds.

Sensitivity analyses of lead lag modes are conducted with respect to air density and steady-state coning angle, see Fig. 12. Looking at this figure one can see that varying the air density from −30% to +30%, around sea level and 15 °C of temperature ($\rho = 1.225$ kg/m^3), results in small variations in the lag modes damping.

Varying the air density modifies the role of aerodynamic forces and especially the damping they can provide to flap motion. The last seems quite insensitive to altitude or temperature changes. When it comes to the variation of the steady state rotor coning angle β_{0ss}, it can be seen the damping of lag modes is very sensitive to this value, a deeper understanding of why this happens is proposed in the next section.

3.2. Understanding the mechanisms of lead-lag instability

The above analysis of the coupled vehicle–pilot biodynamics suggests that:

1) Low frequency roll axis instability involving pilot biodynamics in lateral tasks is the result of a destabilization of both regressing and advancing lag modes;
2) The damping of the regressing lag mode decreases especially when the pilot biodynamics mode frequency is lower than the regressing lag mode frequency;
3) Whatever the positioning of the pilot biodynamics mode frequency is, the advancing lag mode damping seems to be affected by pilot biodynamics;
4) The destabilization of both vehicle lag modes is very sensitive to the steady state rotor coning angle.

The mechanism of lead-lag instability involving pilot biodynamics will be next explained using two approaches: 1) Campbell diagrams and 2) Force phasing matrices [24].

3.2.1. Campbell diagrams applied to the roll axis instability problem through BDFT lateral cyclic inputs

Generally, Campbell diagrams give the representation of the system eigenvalues as a function of rotor angular velocity. In the upper part of the diagram, one can see potential coalescences of the system modes frequencies and on the lower part the damping evolution in the system. Fig. 11 plots the Campbell diagrams of the pilot–vehicle system in three cases: baseline pilot biodynamics, stiffer pilot and a relaxed pilot. Looking at this figure one can see that, for the baseline pilot, the pilot biodynamics mode intersects first both the regressing and advancing lag modes (point A) and further away, at a higher rpm, it intersects again only the regressing lag (point B). Looking at the lag damping in this case, it appears that pilot biodynamics has little impact on the lag modes and therefore one can conclude that pilot biodynamics is not triggering a dangerous PAO problem. However, when the pilot gets 'Stiffer', there is an intersection between the pilot mode and the advancing flap mode which is causing the destabilization of the advancing lag mode (see point C in Fig. 11). In this case, there seems to be continuously an "issue" for the advancing flap mode frequency, as its frequency grows very fast with Ω when compared to the regressing lag mode frequency increase. As a result, the pilot biodynamics will *always* cross the advancing lag mode and therefore unwillingly excite the advancing lag mode. Of course, for relatively small pilot biodynamics gains, the lower the Ω, the less energy is involved in the instability and the lesser will be the impact on the system. This is the case of the 'Relaxed' pilot (see point E and F in Fig. 11), one can see that when there is an intersection of the pilot biodynamics mode with both advancing flap
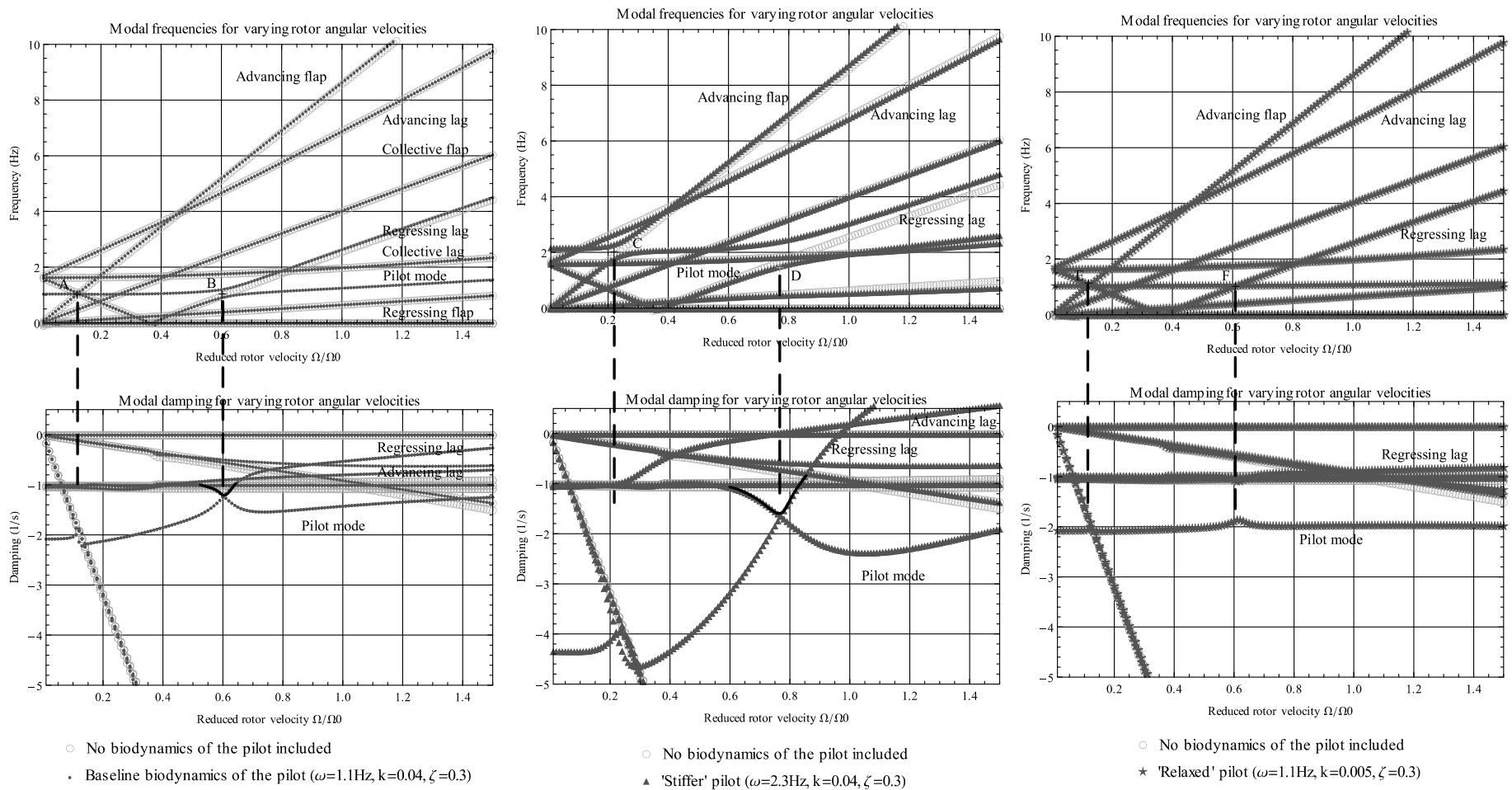
Fig. 11. Campbell diagrams deviations from no pilot in the loop to three different pilot behaviors.
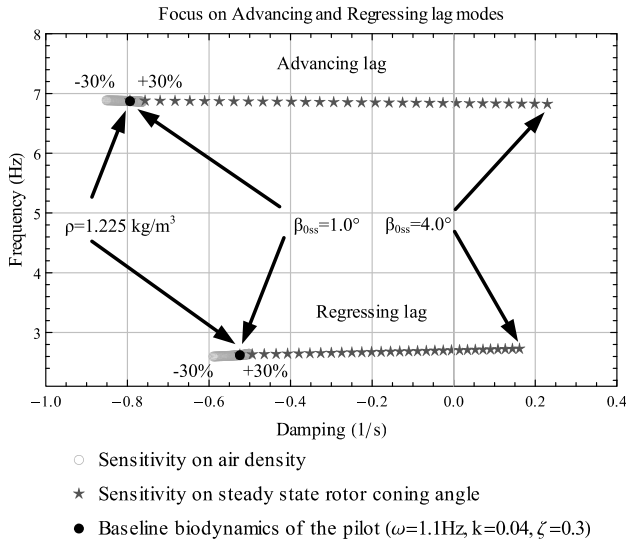
Fig. 12. Sensitivity to air density and steady state rotor coning angle.

and regressing lag modes, but the damping of the both lag modes remains almost unaffected. The physical explanation of advancing lead-lag mode branch intersecting the pilot mode and destabilizing it is given in the next section of this chapter using energetic method explaining the forces involved in the system and their vicious circles of energy flow.

Furthermore, representing the regressing lag mode eigenvectors, see Fig. 13, it appears that, for the stiffer pilot (white bars), the flapping motion couples more strongly to the lead lag motion than in the case of baseline pilot biodynamics. One should recall that the helicopter roll motion is obtained by modifying the rotor thrust orientation, i.e. by generating cyclic flapping motion. Also, recalling Fig. 6, it follows that in the presence of pilot biodynamics, the advancing and regressing lag modes are not only composed of a coupling between lateral/roll, flap and lag motions but also it involves lateral cyclic lever motion (this last state being a new variable associated with the pilot motion).

Concluding, for a stiffer pilot, the pilot biodynamics mode intersects the regressing lag mode and leads to a loss of damping of this mode. This mechanism is very similar to the ground resonance phenomenon coupling, where the weakly damped regressing lag mode couples to the airframe roll movement on its landing gear [15]. The difference between the ground resonance scenario and the roll axis instability through pilot cyclic control is that the pilot biodynamics gain dictates the loss of damping in the regressing lag mode.

3.2.2. Force phasing matrices applied to the roll axis instability problem through BDFT cyclic inputs

The so-called "energy flow" or "forcing phasing matrices (FPM)" analysis [24] (Appendix B) will be next applied to the roll axis instability. According to this method, a dynamic instability is equiva-

lent with at least one energy-flow path wherein two or more system's degrees of freedom mutually pump energy into each other with ever increasing amplitude [24]. The FPM method can be applied to both linear time invariant and time periodic systems. The following steps should be followed:

1) Identify the most active degree(s) of freedom in the eigenvectors modal shapes;
2) Search for the highest positive values in the FPM representing the most active dof. These are the so-called "critical forces";
3) Search for the critical forces positions in the mass, damping and stiffness matrices. These forces are off-diagonal forces that are almost in phase with velocity vector and thus pump energy into a given dof. The positive sign of a term in the mass, damping or stiffness matrices of the FPM system means that the corresponding term (which becomes force once it is multiplied by the corresponding state variable) is destabilizing the system.

If there are degrees of freedom which mutually pump energy into each other, this indicates the possibility of dynamic instability. The FPM method was applied to the helicopter roll axis instability through BDFT lateral cyclic inputs. First, from Fig. 13 it appears that the most active degrees of freedom in the eigenvectors modal shapes correspond to advancing and regressing lag modes. Using the 'Stiffer' pilot parameters ($\omega = 2.3$ Hz, $k = 0.04$) for which the two lag modes have been proved to be unstable, the highest positive values in the FPM were searched. The FPM values are calculated in Appendix B (Eqns. (B.9)–(B.14)) for both regressing and advancing lag modes. Three energy circles are present in the system when analyzing the regressing lag mode: lateral x to roll α_y motions, flap $\beta_{1c,1s}$ to roll α_y and flap $\beta_{1c,1s}$ to lag $\delta_{1c,1s}$, see Fig. 14 for the generic representation of the system and Appendix B for the numerical values. Appendix B highlights also the critical driving forces in the system. These reveal that two symmetric off-diagonal terms of the FPMs have positive values. Therefore, vicious energy cycle loops appear, see Fig. 14. Observe that in the case of advancing lag mode, the energy flow loop between lateral x and roll α_y dofs is not present.

The expressions of the driving forces responsible for the energy flow circles are given in Table 3. For both regressing and advancing lag modes, there are two critical forces in the first line of the mass matrix M that do not create any energy loop, i.e. $(4hm_{bl} + m_s\beta_{0ss})\dot{\alpha}_y$ and $(2m_s\beta_{0ss})\ddot{\beta}_{1s}$. As these both critical forces are in the first line of mass matrix M, it follows that these two forces drive energy into the lateral translation x dof; this is precisely the acceleration that will excite pilot biodynamics feedthrough.

The pilot is indirectly participating to the instability by inputting energy into the flap motion, term $m_{10,1}$ in Fig. 14. He/she is destabilizing both the advancing and regressing lag modes by destabilizing the flap-roll and flap-lag couplings.

One can identify that, in the case of regressing lag mode, this driving force is of aerodynamic nature for both lateral-roll and
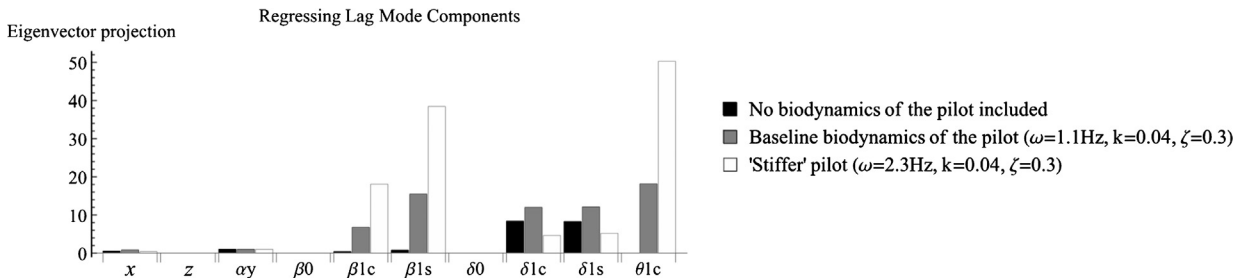
Fig. 13. Regressing lag modal shape when varying pilot biodynamics.
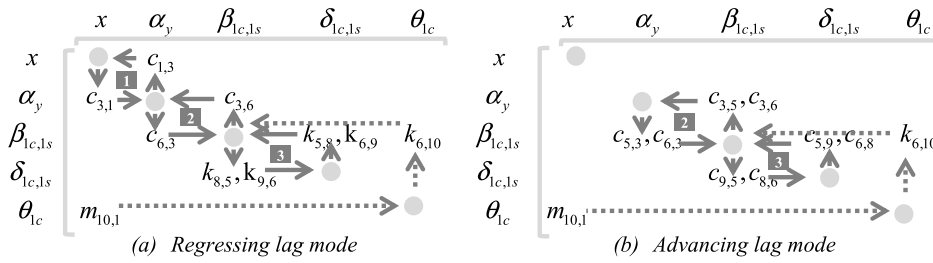
Fig. 14. Critical drivers and energy-flow paths.

Table 3
Driving forces in the energy circles.

	Regressing lag mode	Advancing lag mode
1: Lateral-roll	$c_{1,3}.\ddot{\alpha}_y = \frac{I_{bl}(3e+2R)\beta_{0ss}\gamma\Omega}{6R^2}.\ddot{\alpha}_y$	–
2: Flap-roll	$c_{3,6}.\dot{\beta}_{1s} = \frac{I_{bl}(4e+3R+4h\beta_{0ss})\gamma\Omega}{12R}.\dot{\beta}_{1s}$	$c_{3,6}.\dot{\beta}_{1s} = \frac{I_{bl}(4e+3R+4h\beta_{0ss})\gamma\Omega}{12R}.\dot{\beta}_{1s}$ $c_{3,5}.\dot{\beta}_{1c} = -4(I_{bl}+em_s)\Omega.\dot{\beta}_{1c}$
3: Flap-lag	$k_{8,5}.\beta_{1c} = 4I_{bl}\beta_{0ss}\Omega^2.\beta_{1c}$	$c_{9,5}.\dot{\beta}_{1c} = 4I_{bl}\beta_{0ss}\Omega.\dot{\beta}_{1c}$

flap-roll couplings; in the case of advancing lag mode, the driving force in flap-roll coupling is of aerodynamic nature as well. For the flap-lag coupling, the driving force is due to the Coriolis effect for both advancing and regressing lag modes. From the magnitude of Coriolis forces in the flap to lag and lag to flap coupling terms of the FPM matrices, one can see that the transfer from flap to lag is ten times higher in magnitude than the reverse from lag to flap. Neglecting the term $4h\beta_{0ss}$ in the flap-roll coupling as it is very small when compared to $4e+3R$, one can say that the lateral-roll coupling depends on the $\beta_{0ss}\gamma$ product, the flap-roll coupling depends on the Lock number γ and the flap-lag coupling depends on the coning angle β_{0ss}. Recalling the sensitivity analysis on air density and steady state rotor coning angle presented in Fig. 12, it follows that the variation of β_{0ss} is furthermost the most critical factor in the variation of damping for both regressing and advancing lag modes. As a result, the most destabilizing forces in the FPM matrices are the Coriolis forces from flap to lag. The mechanism explained herein for the pilot biodynamics is very similar to the one of air resonance [15,16]. If one examines the critical force associated to pilot action $m_{10,1}$, it appears that the power input from the pilot is proportional to $k\omega^2$ multiplied by the airframe lateral acceleration $\ddot{x}$. As a result, the more a pilot is in a stressful situation or in a task that demands his/her neuromuscular system to adapt to a 'Stiffer' configuration (Fig. 10), both pilot gain k and pilot resonant frequency ω will increase and the energy he/she will transfer to the system will increase proportionally to $k\omega^2$. Minimizing the above critical forces in the FPM matrices will help recovering some damping of the unstable modes but it cannot suppress the roll axis instability phenomenon.

4. Conclusion

The goal of the present paper was to explain the mechanism of roll axis instability through pilot BDFT lateral cyclic inputs for soft-inplane rotors. It is known that these rotors are more critical to biodynamic couplings and unstable PAOs. Using an identified pilot biodynamics model and coupling it to the critical dofs involved in the instability (i.e. lateral, vertical and roll degrees of freedom for the fuselage and flap, lag and pitch for the blades) the paper demonstrated that *both* the lightly damped regressing lag mode and the advancing lag mode participate to the instability. Usually, the literature of specialty relates only to the regressing lag mode as this is close to the pilot's biodynamics mode. The paper demonstrates that the advancing lag mode is crucial for the

roll axis instability through pilot lateral cyclic and should be included in the analysis especially in the case of a soft-inplane rotor. The mechanism of destabilization is slightly different for the two modes: while regressing lag mode recovers its damping when pilot neuromuscular adaption varies to a stiffer pilot, the advancing lag mode is unable to recover its damping being very little damped for a Stiff pilot. From energetic point of view, three vicious energy circles have been identified for the regressing lag mode (in a similar manner as for the air resonance instability): lateral-roll, flap-roll and flap-lag. Furthermore, for the advancing lag mode, two vicious energy circles exist: flap-roll and flap-lag. This shows that pilot biodynamics can input energy to higher order modes, usually not involved in the instability. For the roll axis instability problem through BDFT lateral cyclic inputs, the pilot is indirectly participating to the instability by inputting energy into the flap motion, which is transmitted further to both advancing and regressing lag modes. As the advancing lag mode is not recovering damping, it will be the first one to become unstable. For both lag modes, the destabilization is very sensitive to an increase in the steady state rotor coning angle; this increases the energy transfers from flap to lag motion through Coriolis forces. Future work will implement more complex aerodynamics to investigate the roll axis instability phenomenon at higher helicopter speeds. Also, future studies may investigate the development of an adapted flight control system and filter design considering the effect of advancing lag mode to alleviate lateral-roll aeroelastic RPCs.

Conflict of interest statement

No confict of interest.

Appendix A

The equations of motion of air resonance model for roll axis helicopter instability are:

x	$-\dfrac{I_{bl}\beta_{0ss}\gamma\Omega^2\beta_{1c}}{3R} - \dfrac{I_{bl}\beta_{0ss}\gamma\Omega^2\theta_{1s}}{3R} + \dfrac{eI_{bl}\beta_{0ss}\gamma\Omega\alpha'_y}{2R^2} + \dfrac{I_{bl}\beta_{0ss}\gamma\Omega\alpha'_y}{3R} + \dfrac{I_{bl}\beta_{0ss}\gamma\Omega\beta'_{1s}}{3R} + M_f x'' + 4M_{bl}x'' + 4hM_{bl}\alpha''_y + 4m_s\beta_{0ss}\alpha''_y + 2m_s\beta_{0ss}\beta''_{1s} - 2m_s\delta''_{1c} = 0$	(A.1)

z	$-\dfrac{eI_{bl}\beta_{0ss}\gamma\Omega^2\delta_0}{R^2} - \dfrac{2I_{bl}\gamma\Omega^2\theta_0}{3R} + \dfrac{I_{bl}\gamma\Omega z'}{R^2} + \dfrac{2I_{bl}\gamma\Omega\beta'_0}{3R} + M_f z'' + 4M_{bl}z'' + 4m_s\beta''_0 = 0$	(A.2)

α_y	$-\dfrac{1}{4}I_{bl}\gamma\Omega^2\beta_{1c} - \dfrac{eI_{bl}\gamma\Omega^2\beta_{1c}}{3R} - \dfrac{hI_{bl}\beta_{0ss}\gamma\Omega^2\beta_{1c}}{3R} - \dfrac{e^2I_{bl}\beta_{0ss}\gamma\Omega^2\delta_{1s}}{2R^2} - \dfrac{eI_{bl}\beta_{0ss}\gamma\Omega^2\delta_{1s}}{3R} - \dfrac{1}{4}I_{bl}\gamma\Omega^2\theta_{1s} - \dfrac{eI_{bl}\gamma\Omega^2\theta_{1s}}{3R} - \dfrac{hI_{bl}\beta_{0ss}\gamma\Omega^2\theta_{1s}}{3R} + \dfrac{eI_{bl}\gamma\Omega x'}{2R^2}$ $+ \dfrac{I_{bl}\beta_{0ss}\gamma\Omega x'}{3R} + \dfrac{1}{4}I_{bl}\gamma\Omega\alpha'_y + \dfrac{e^2I_{bl}\gamma\Omega\alpha'_y}{2R^2} + \dfrac{2eI_{bl}\gamma\Omega\alpha'_y}{3R} + \dfrac{ehI_{bl}\beta_{0ss}\gamma\Omega\alpha'_y}{R^2} + \dfrac{2hI_{bl}\beta_{0ss}\gamma\Omega\alpha'_y}{3R} - 4I_{bl}\Omega\beta'_{1c} - 4em_s\Omega\beta'_{1c} + \dfrac{1}{4}I_{bl}\gamma\Omega\beta'_{1s} + \dfrac{eI_{bl}\gamma\Omega\beta'_{1s}}{3R}$ $+ \dfrac{hI_{bl}\beta_{0ss}\gamma\Omega\beta'_{1s}}{3R} + 4hM_{bl}x'' + 4m_s\beta_{0ss}x'' + 2I_{bl}\alpha''_y + I_{yy}\alpha''_y + 2e^2M_{bl}\alpha''_y + 4h^2M_{bl}\alpha''_y + 4em_s\alpha''_y + 8hm_s\beta_{0ss}\alpha''_y + 2I_{bl}\beta''_{1s} + 2em_s\beta''_{1s}$ $+ 2hm_s\beta_{0ss}\beta''_{1s} - 2hm_s\delta''_{1c} - 2I_{bl}\beta_{0ss}\delta''_{1c} = 0$	(A.3)

β_0	$4I_{bl}\Omega^2\beta_0 + 4em_s\Omega^2\beta_0 - \dfrac{2eI_{bl}\beta_{0ss}\gamma\Omega^2\delta_0}{3R} - \dfrac{1}{2}I_{bl}\gamma\Omega^2\theta_0 + \dfrac{2I_{bl}\gamma\Omega z'}{3R} + \dfrac{1}{2}I_{bl}\gamma\Omega\beta'_0 + 8I_{bl}\beta_{0ss}\Omega\delta'_0 + 4m_s z'' + 4I_{bl}\beta''_0 = 0$	(A.4)

β_{1c}	$-\dfrac{1}{4}I_{bl}\gamma\Omega^2\beta_{1c} + 2em_s\Omega^2\beta_{1s} - 4I_{bl}\beta_{0ss}\Omega^2\delta_{1c} - \dfrac{eI_{bl}\beta_{0ss}\gamma\Omega^2\delta_{1s}}{3R} - \dfrac{1}{4}I_{bl}\gamma\Omega^2\theta_{1s} + \dfrac{I_{bl}\beta_{0ss}\gamma\Omega x'}{3R} + \dfrac{1}{4}I_{bl}\gamma\Omega\alpha'_y + \dfrac{eI_{bl}\gamma\Omega\alpha'_y}{3R} + \dfrac{hI_{bl}\beta_{0ss}\gamma\Omega\alpha'_y}{3R}$ $- 4I_{bl}\Omega\beta'_{1c} + \dfrac{1}{4}I_{bl}\gamma\Omega\beta'_{1s} + 4I_{bl}\beta_{0ss}\Omega\delta'_{1s} + 2m_s\beta_{0ss}x'' + 2I_{bl}\alpha''_y + 2em_s\alpha''_y + 2hm_s\beta_{0ss}\alpha''_y + 2I_{bl}\beta''_{1s} = 0$	(A.5)

β_{1s}	$-2em_s\Omega^2\beta_{1c} - \dfrac{1}{4}I_{bl}\gamma\Omega^2\beta_{1s} + \dfrac{eI_{bl}\beta_{0ss}\gamma\Omega^2\delta_{1c}}{3R} - 4I_{bl}\beta_{0ss}\Omega^2\delta_{1s} + \dfrac{1}{4}I_{bl}\gamma\Omega^2\theta_{1c}$ $- 4I_{bl}\Omega\alpha'_y - 4em_s\Omega\alpha'_y - \dfrac{1}{4}I_{bl}\gamma\Omega\beta'_{1c} - 4I_{bl}\Omega\beta'_{1s} - 4I_{bl}\beta_{0ss}\Omega\delta'_{1c} - 2I_{bl}\beta''_{1c} = 0$	(A.6)

δ_0	$4k_\delta\delta_0 + 4em_s\Omega^2\delta_0 - 8I_{bl}\beta_{0ss}\Omega\beta'_0 + 4c_\delta\delta'_0 + 4I_{bl}\delta''_0 = 0$	(A.7)

δ_{1c}	$4I_{bl}\beta_{0ss}\Omega^2\beta_{1c} - 2c_\delta\Omega\delta_{1c} + 2k_\delta\delta 1s - 2I_{bl}\Omega^2\delta_{1s} + 2em_s\Omega^2\delta_{1s} - 4I_{bl}\beta_{0ss}\Omega\beta'_{1s} - 4I_{bl}\Omega\delta'_{1c} + 2c_\delta\delta'_{1s} + 2I_{bl}\delta''_{1s} = 0$	(A.8)

δ_{1s}	$4I_{bl}\beta_{0ss}\Omega^2\beta_{1s} - 2k_\delta\delta_{1c} + 2I_{bl}\Omega^2\delta_{1c} - 2em_s\Omega^2\delta_{1c} - 2c_\delta\Omega\delta_{1s} + 4I_{bl}\beta_{0ss}\Omega\beta'_{1c} - 2c_\delta\delta'_{1c} - 4I_{bl}\Omega\delta'_{1s} + 2m_s x'' + 2hm_s\alpha''_y + 2I_{bl}\beta_{0ss}\alpha''_y - 2I_{bl}\delta''_{1c} = 0$	(A.9)

Using the matrix notation and adding the pilot biodynamics to the vehicle motion, this gives the final matrix formulation of the roll axis instability problem as:

$$M\ddot{q} + C\dot{q} + Kq = 0 \qquad (A.10)$$

where $\boldsymbol{q} = [x, z, \alpha_y, \beta_0, \beta_{1c}, \beta_{1s}, \delta_0, \delta_{1c}, \delta_{1s}, \theta_{1c}]^T$ represents the state vector and M, C and K respectively the mass, damping and stiffness matrices. Their expressions are:

$$\boldsymbol{M} = \begin{bmatrix} M_f + 4M_{bl} & 0 & 4(hM_{bl} + m_s\beta_{0ss}) \\ 0 & M_f + 4M_{bl} & 0 \\ 4(hM_{bl} + m_s\beta_{0ss}) & 0 & 2I_{bl} + I_{yy} + 2e^2M_{bl} + 4h^2M_{bl} + 4em_s + 8hm_s\beta_{0ss} \\ 0 & 4ms & 0 \\ 2m_s\beta_{0ss} & 0 & 2(I_{bl} + m_s(e + h\beta_{0ss})) \\ 0 & 0 & 0 \\ 0 & 0 & 0 \\ 0 & 0 & 0 \\ 2m_s & 0 & 2(hm_s + I_{bl}\beta_{0ss}) \\ k\omega^2 & 0 & 0 \end{bmatrix}$$

$$\begin{bmatrix} 0 & 0 & 2m_s\beta_{0ss} & 0 & -2m_s & 0 & 0 \\ 4m_s & 0 & 0 & 0 & 0 & 0 & 0 \\ 0 & 0 & 2(I_{bl} + m_s(e + h\beta_{0ss})) & 0 & -2(hm_s + I_{bl}\beta_{0ss}) & 0 & 0 \\ 4I_{bl} & 0 & 0 & 0 & 0 & 0 & 0 \\ 0 & 0 & 2I_{bl} & 0 & 0 & 0 & 0 \\ 0 & -2I_{bl} & 0 & 0 & 0 & 0 & 0 \\ 0 & 0 & 0 & 4I_{bl} & 0 & 0 & 0 \\ 0 & 0 & 0 & 0 & 0 & 2I_{bl} & 0 \\ 0 & 0 & 0 & 0 & -2I_{bl} & 0 & 0 \\ 0 & 0 & 0 & 0 & 0 & 0 & -G \end{bmatrix} \qquad (A.11)$$

$$\boldsymbol{C} = \begin{bmatrix} 0 & 0 & \dfrac{I_{bl}(3e+2R)\beta_{0ss}\gamma\Omega}{6R^2} & 0 \\ 0 & \dfrac{I_{bl}\gamma\Omega}{R^2} & 0 & \dfrac{2I_{bl}\gamma\Omega}{3R} \\ \dfrac{I_{bl}(3e+2R)\beta_{0ss}\gamma\Omega}{6R^2} & 0 & \dfrac{I_{bl}(6e^2+8eR+3R^2+12eh\beta_{0ss}+8hR\beta_{0ss})\gamma\Omega}{12R^2} & 0 \\ 0 & \dfrac{2I_{bl}\gamma\Omega}{3R} & 0 & \dfrac{I_{bl}\gamma\Omega}{2} \\ \dfrac{I_{bl}\beta_{0ss}\gamma\Omega}{3R} & 0 & \dfrac{I_{bl}(4e+3R+4h\beta_{0ss})\gamma\Omega}{12R} & 0 \\ 0 & 0 & -4(I_{bl} + em_s)\Omega & 0 \\ 0 & 0 & 0 & -8I_{bl}\beta_{0ss}\Omega \\ 0 & 0 & 0 & 0 \\ 0 & 0 & 0 & 0 \\ 0 & 0 & 0 & 0 \end{bmatrix}$$

$$\left.\begin{array}{cccccc}
0 & \frac{I_{bl}\beta_{0ss}\gamma\Omega}{3R} & 0 & 0 & 0 & 0 \\
0 & 0 & 0 & 0 & 0 & 0 \\
-4(I_{bl}+em_s)\Omega & \frac{I_{bl}(4e+3R+4h\beta_{0ss})\gamma\Omega}{12R} & 0 & 0 & 0 & 0 \\
0 & 0 & 8I_{bl}\beta_{0ss}\Omega & 0 & 0 & 0 \\
-4I_{bl}\Omega & \frac{I_{bl}\gamma\Omega}{4} & 0 & 0 & 4I_{bl}\beta_{0ss}\Omega & 0 \\
-\frac{1}{4}I_{bl}\gamma\Omega & -4I_{bl}\Omega & 0 & -4I_{bl}\beta_{0ss}\Omega & 0 & 0 \\
0 & 0 & 4c_\delta & 0 & 0 & 0 \\
0 & -4I_{bl}\beta_{0ss}\Omega & 0 & -4I_{bl}\Omega & 2c_\delta & 0 \\
4I_{bl}\beta_{0ss}\Omega & 0 & 0 & -2c_\delta & -4I_{bl}\Omega & 0 \\
0 & 0 & 0 & 0 & 0 & -2G\zeta\omega
\end{array}\right] \tag{A.12}$$

$$\boldsymbol{K} = \left[\begin{array}{ccccc}
0 & 0 & 0 & 0 & -\frac{I_{bl}\beta_{0ss}\gamma\Omega^2}{3R} & 0 \\
0 & 0 & 0 & 0 & 0 & 0 \\
0 & 0 & 0 & 0 & -\frac{I_{bl}(4e+3R+4h\beta_{0ss})\gamma\Omega^2}{12R} & 0 \\
0 & 0 & 0 & 4(I_{bl}+em_s)\Omega^2 & 0 & 0 \\
0 & 0 & 0 & 0 & -\frac{1}{4}I_{bl}\gamma\Omega^2 & 2em_s\Omega^2 \\
0 & 0 & 0 & 0 & -2em_s\Omega^2 & -\frac{1}{4}I_{bl}\gamma\Omega^2 \\
0 & 0 & 0 & 0 & 0 & 0 \\
0 & 0 & 0 & 0 & 4I_{bl}\beta_{0ss}\Omega^2 & 0 \\
0 & 0 & 0 & 0 & 0 & 4I_{bl}\beta_{0ss}\Omega^2 \\
0 & 0 & 0 & 0 & 0 & 0
\end{array}\right.$$

$$\left.\begin{array}{cccc}
0 & 0 & 0 & 0 \\
-\frac{eI_{bl}\beta_{0ss}\gamma\Omega^2}{R^2} & 0 & 0 & 0 \\
0 & 0 & -\frac{eI_{bl}(3e+2R)\beta_{0ss}\gamma\Omega^2}{6R^2} & 0 \\
-\frac{2eI_{bl}\beta_{0ss}\gamma\Omega^2}{3R} & 0 & 0 & 0 \\
0 & -4I_{bl}\beta_{0ss}\Omega^2 & -\frac{eI_{bl}\beta_{0ss}\gamma\Omega^2}{3R} & 0 \\
0 & \frac{eI_{bl}\beta_{0ss}\gamma\Omega^2}{3R} & -4I_{bl}\beta_{0ss}\Omega^2 & \frac{1}{4}I_{bl}\gamma\Omega^2 \\
4(k_\delta+em_s\Omega^2) & 0 & 0 & 0 \\
0 & -2c_\delta\Omega & 2(k_\delta+(-I_{bl}+em_s)\Omega^2) & 0 \\
0 & -2(k_\delta+(-I_{bl}+em_s)\Omega^2) & -2c_\delta\Omega & 0 \\
0 & 0 & 0 & -G\omega^2
\end{array}\right] \tag{A.13}$$

Appendix B. Force-phasing matrices approach

The computation of force phasing matrices is done by introducing the kth eigenvector of A associated to its eigenvalue. By reintroducing the eigenvector $\{\phi^{(k)}\}$ associated to its eigenvalue λ_k as a general solution of the homogeneous equations of motion,

$$\mathbf{x} = \sum e^{\lambda_k}\cdot\{\phi^{(k)}\} \tag{B.1}$$

The equations of motion using the kth eigenvector can be expressed as,

$$m_{nn}\lambda_k^2\phi_n^{(k)} + c_{nn}\lambda_k\phi_n^{(k)} + k_{nn}\phi_n^{(k)}$$
$$+ \underbrace{\sum_{j\neq n}(m_{nj}\lambda_k^2 + c_{nj}\lambda_k + k_{nj})\phi_j^{(k)}}_{f_n} = 0 \tag{B.2}$$

Once represented in the complex plane, equation (B.2) leads to Fig. 15. These vectors can be obtained by computing the so-called "force-phasing matrices" (FPMs) [24]. The technique consists in normalizing $\boldsymbol{M}$, $\boldsymbol{C}$, $\boldsymbol{K}$ matrices by the damper forces, see equations (B.3) to (B.8). The sign of each term, in each force phasing matrix gives the orientation of each one of the forces in the equations of motion in the complex plane.

Such normalization allows to align the damper forces (diagonal terms of the damping matrix) with the real axis with a magnitude of 1 while being in the left hand part of the complex plane. The inertia and spring forces are the diagonal terms of the mass and stiffness matrix. For each line of the matrices, the positive off-diagonal terms are the driving forces (f_n), see Fig. 15. If these terms are positive, then a projection of the driving force is in phase with the velocity: the work of this force on the system through a given degree of freedom is positive and acts as a contributor to the destabilization of the system. The identification of the driving
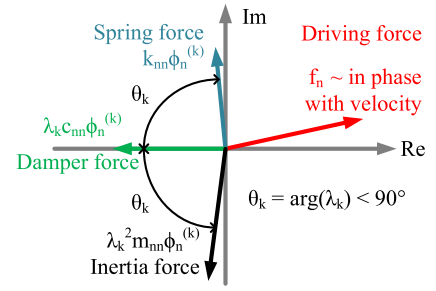
Fig. 15. Driving forces in the complex plane.

forces is done only for the most active degrees of freedom that are obtained from the modal shape of the unstable mode under investigation. Finally, looking for the position of these terms in the original mass, damping and stiffness matrices allows obtaining the analytical expressions of the critical forces.

$$[P_M^{(k)}] = [p_{M_{ij}}^{(k)}] = -\mathrm{Re}\left[[m_{ij}]\otimes\left[\frac{\alpha_j^{(k)}}{\beta_i^{(k)}c_{ii}}\right]\right] \tag{B.3}$$

$$[P_C^{(k)}] = [p_{C_{ij}}^{(k)}] = -\mathrm{Re}\left[[c_{ij}]\otimes\left[\frac{\beta_j^{(k)}}{\beta_i^{(k)}c_{ii}}\right]\right] \tag{B.4}$$

$$[P_K^{(k)}] = [p_{K_{ij}}^{(k)}] = -\mathrm{Re}\left[[k_{ij}]\otimes\left[\frac{\gamma_j^{(k)}}{\beta_i^{(k)}c_{ii}}\right]\right] \tag{B.5}$$

where the $\otimes$ symbol denotes the Hadamard or term by term matrix multiplication [24]. The complex-valued $\alpha^{(k)}$, $\beta^{(k)}$ and $\gamma^{(k)}$ are formed from the results of the basic eigensolution:

$$\{\alpha^{(k)}\} = \lambda_k^2\{\varphi^{(k)}\} \tag{B.6}$$

$$\{\beta^{(k)}\} = \lambda_k\{\varphi^{(k)}\} \tag{B.7}$$

$$\{\gamma^{(k)}\} = \{\varphi^{(k)}\} \tag{B.8}$$

Regressing lag mode

$[P_M] =$

	x	z	alpha y	beta0	beta1c	bet1as	lag0	lag1c	lag1s	theta1c
x	-1,60E+03	0,00E+00	1,34E+04	0,00E+00	0,00E+00	-5,11E+03	0,00E+00	4,69E+03	0,00E+00	0,00E+00
z	0,00E+00	-2,30E-01	0,00E+00	-4,56E-01	0,00E+00	0,00E+00	0,00E+00	0,00E+00	0,00E+00	0,00E+00
alpha y	-1,71E-02	0,00E+00	-2,77E-02	0,00E+00	0,00E+00	-1,44E+00	0,00E+00	2,90E-01	0,00E+00	0,00E+00
beta0	0,00E+00	1,27E-01	0,00E+00	-6,20E-03	0,00E+00	0,00E+00	0,00E+00	0,00E+00	0,00E+00	0,00E+00
beta1c	2,00E-05	0,00E+00	-1,87E-02	0,00E+00	0,00E+00	6,56E-01	0,00E+00	0,00E+00	0,00E+00	0,00E+00
bet1as	0,00E+00	0,00E+00	0,00E+00	0,00E+00	1,44E-01	0,00E+00	0,00E+00	0,00E+00	0,00E+00	0,00E+00
lag0	0,00E+00	0,00E+00	0,00E+00	0,00E+00	0,00E+00	0,00E+00	-1,01E-01	0,00E+00	0,00E+00	0,00E+00
lag1c	0,00E+00	0,00E+00	0,00E+00	0,00E+00	0,00E+00	0,00E+00	0,00E+00	0,00E+00	3,74E-01	0,00E+00
lag1s	-4,96E-03	0,00E+00	2,55E-02	0,00E+00	0,00E+00	0,00E+00	0,00E+00	2,97E-01	0,00E+00	0,00E+00
theta1c	4,96E-01	0,00E+00	0,00E+00	0,00E+00	0,00E+00	0,00E+00	0,00E+00	0,00E+00	0,00E+00	-4,88E-02

(B.9)

$[P_C] =$

	x	z	alpha y	beta0	beta1c	bet1as	lag0	lag1c	lag1s	theta1c
		Lateral - roll			Flap- roll					
x	0,00E+00	0,00E+00	7,91E+02	0,00E+00	0,00E+00	-2,94E+04	0,00E+00	0,00E+00	0,00E+00	0,00E+00
z	0,00E+00	-1,00E+00	0,00E+00	1,69E+00	0,00E+00	0,00E+00	0,00E+00	0,00E+00	0,00E+00	0,00E+00
alpha y	1,07E-03	0,00E+00	-1,00E+00	0,00E+00	-9,69E+00	3,62E+01	0,00E+00	0,00E+00	0,00E+00	0,00E+00
beta0	0,00E+00	4,48E-01	0,00E+00	-1,00E+00	0,00E+00	0,00E+00	-1,67E-01	0,00E+00	0,00E+00	0,00E+00
beta1c	2,25E-05	0,00E+00	-1,05E-02	0,00E+00	-1,00E+00	4,68E-01	0,00E+00	0,00E+00	-4,04E-03	0,00E+00
bet1as	0,00E+00	0,00E+00	2,75E-02	0,00E+00	-1,03E-01	1,00E+00	0,00E+00	-2,05E-03	0,00E+00	0,00E+00
lag0	0,00E+00	0,00E+00	0,00E+00	3,42E-02	0,00E+00	0,00E+00	-1,00E+00	0,00E+00	0,00E+00	0,00E+00
lag1c	0,00E+00	0,00E+00	0,00E+00	0,00E+00	0,00E+00	-1,42E-01	0,00E+00	-1,00E+00	3,90E-04	0,00E+00
lag1s	0,00E+00	0,00E+00	0,00E+00	0,00E+00	-4,90E-02	0,00E+00	0,00E+00	-3,09E-04	-1,00E+00	0,00E+00
theta1c	0,00E+00	0,00E+00	0,00E+00	0,00E+00	0,00E+00	0,00E+00	0,00E+00	0,00E+00	0,00E+00	-1,00E+00

(B.10)

$[P_K] =$

	x	z	alpha y	beta0	beta1c	bet1as	lag0	lag1c	lag1s	theta1c
x	0,00E+00	0,00E+00	0,00E+00	0,00E+00	1,71E+04	0,00E+00	0,00E+00	0,00E+00	0,00E+00	0,00E+00
z	0,00E+00	0,00E+00	0,00E+00	0,00E+00	0,00E+00	0,00E+00	-2,49E-02	0,00E+00	0,00E+00	0,00E+00
alpha y	0,00E+00	0,00E+00	0,00E+00	0,00E+00	-2,43E+01	0,00E+00	0,00E+00	0,00E+00	6,49E-03	0,00E+00
beta0	0,00E+00	0,00E+00	0,00E+00	-1,48E-02	0,00E+00	0,00E+00	1,00E-02	0,00E+00	0,00E+00	0,00E+00
beta1c	0,00E+00	0,00E+00	0,00E+00	0,00E+00	-8,82E-03	-8,77E-02	0,00E+00	5,39E-03	1,35E-04	0,00E+00
bet1as	0,00E+00	0,00E+00	0,00E+00	0,00E+00	-1,95E-02	-8,82E-03	0,00E+00	2,1?E-05	3,43E-03	9,59E-01
lag0	0,00E+00	0,00E+00	0,00E+00	0,00E+00	0,00E+00	0,00E+00	-4,25E-02	0,00E+00	0,00E+00	0,00E+00
lag1c	0,00E+00	0,00E+00	0,00E+00	0,00E+00	8,36E-02	0,00E+00	0,00E+00	-3,41E-04	6,84E-01	0,00E+00
lag1s	0,00E+00	0,00E+00	0,00E+00	0,00E+00	0,00E+00	1,89E-01	0,00E+00	-5,13E-01	-3,41E-04	0,00E+00
theta1c	0,00E+00	0,00E+00	0,00E+00	0,00E+00	0,00E+00	0,00E+00	0,00E+00	0,00E+00	0,00E+00	-6,23E-03

Pilot to flap

Flap - lag

(B.11)

Advancing lag mode

$[P_M] =$

	x	z	alpha y	beta0	beta1c	bet1as	lag0	lag1c	lag1s	theta1c
x	-1,65E+03	0,00E+00	1,69E+04	0,00E+00	0,00E+00	-2,54E+04	0,00E+00	1,14E+04	0,00E+00	0,00E+00
z	0,00E+00	-2,36E-01	0,00E+00	1,00E+00	0,00E+00	0,00E+00	0,00E+00	0,00E+00	0,00E+00	0,00E+00
alpha y	-5,58E-02	0,00E+00	-2,85E-02	0,00E+00	0,00E+00	-3,70E+01	0,00E+00	1,36E+00	0,00E+00	0,00E+00
beta0	0,00E+00	-2,16E-01	0,00E+00	-6,38E-03	0,00E+00	0,00E+00	0,00E+00	0,00E+00	0,00E+00	0,00E+00
beta1c	-2,60E-05	0,00E+00	-1,97E-02	0,00E+00	0,00E+00	8,47E-01	0,00E+00	0,00E+00	0,00E+00	0,00E+00
bet1as	0,00E+00	0,00E+00	0,00E+00	0,00E+00	5,99E-01	0,00E+00	0,00E+00	0,00E+00	0,00E+00	0,00E+00
lag0	0,00E+00	0,00E+00	0,00E+00	0,00E+00	0,00E+00	0,00E+00	-1,04E-01	0,00E+00	0,00E+00	0,00E+00
lag1c	0,00E+00	0,00E+00	0,00E+00	0,00E+00	0,00E+00	0,00E+00	0,00E+00	0,00E+00	7,33E-01	0,00E+00
lag1s	-1,01E-02	0,00E+00	-3,36E-02	0,00E+00	0,00E+00	0,00E+00	0,00E+00	7,48E-01	0,00E+00	0,00E+00
theta1c	4,91E-01	0,00E+00	0,00E+00	0,00E+00	0,00E+00	0,00E+00	0,00E+00	0,00E+00	0,00E+00	-5,02E-02

(B.12)

$[P_C] =$

	x	z	alpha y	beta0	beta1c	bet1as	lag0	lag1c	lag1s	theta1c
x	0,00E+00	0,00E+00	-5,19E+02	0,00E+00	0,00E+00	4,26E+03	0,00E+00	0,00E+00	0,00E+00	0,00E+00
z	0,00E+00	-1,00E+00	0,00E+00	1,89E+00	0,00E+00	0,00E+00	0,00E+00	0,00E+00	0,00E+00	0,00E+00
alpha y	-1,66E-03	0,00E+00	-1,00E+00	0,00E+00	3,35E+01	1,66E+01	0,00E+00	0,00E+00	0,00E+00	0,00E+00
beta0	0,00E+00	4,18E-01	0,00E+00	-1,00E+00	0,00E+00	0,00E+00	-3,37E-02	0,00E+00	0,00E+00	0,00E+00
beta1c	3,09E-05	0,00E+00	1,4?E-02	0,00E+00	-1,00E+00	1,33E-01	0,00E+00	0,00E+00	2,40E-03	0,00E+00
bet1as	0,00E+00	0,00E+00	1,57E-02	0,00E+00	-1,30E-01	1,00E+00	0,00E+00	9,63E-04	0,00E+00	0,00E+00
lag0	0,00E+00	0,00E+00	0,00E+00	7,25E-02	0,00E+00	0,00E+00	-1,00E+00	0,00E+00	0,00E+00	0,00E+00
lag1c	0,00E+00	0,00E+00	0,00E+00	0,00E+00	0,00E+00	1,49E-02	0,00E+00	0,00E+00	-6,62E-04	0,00E+00
lag1s	0,00E+00	0,00E+00	0,00E+00	0,00E+00	2,68E-02	0,00E+00	0,00E+00	-6,75E-04	-1,00E+00	0,00E+00
theta1c	0,00E+00	0,00E+00	0,00E+00	0,00E+00	0,00E+00	0,00E+00	0,00E+00	0,00E+00	0,00E+00	-1,00E+00

Flap - roll   **Flap - lag**

(B.13)

$[P_K] =$

	x	z	alpha y	beta0	beta1c	bet1as	lag0	lag1c	lag1s	theta1c
x	0,00E+00	0,00E+00	0,00E+00	0,00E+00	-4,96E+03	0,00E+00	0,00E+00	0,00E+00	0,00E+00	0,00E+00
z	0,00E+00	0,00E+00	0,00E+00	0,00E+00	0,00E+00	0,00E+00	-2,88E-03	0,00E+00	0,00E+00	0,00E+00
alpha y	0,00E+00	0,00E+00	0,00E+00	0,00E+00	-1,34E+01	0,00E+00	0,00E+00	0,00E+00	-4,88E-03	0,00E+00
beta0	0,00E+00	0,00E+00	0,00E+00	-3,09E-03	0,00E+00	0,00E+00	1,59E-03	0,00E+00	0,00E+00	0,00E+00
beta1c	0,00E+00	0,00E+00	0,00E+00	0,00E+00	-1,84E-03	-2,31E-02	0,00E+00	-1,71E-03	9,38E-05	0,00E+00
bet1as	0,00E+00	0,00E+00	0,00E+00	0,00E+00	-1,64E-02	-1,84E-03	0,00E+00	8,78E-05	-6,01E-04	5,33E-01
lag0	0,00E+00	0,00E+00	0,00E+00	0,00E+00	-1,84E-02	0,00E+00	-8,87E-03	-1,13E-04	2,72E-01	0,00E+00
lag1c	0,00E+00	0,00E+00	0,00E+00	0,00E+00	-1,84E-02	0,00E+00	0,00E+00	-1,13E-04	2,72E-01	0,00E+00
lag1s	0,00E+00	0,00E+00	0,00E+00	0,00E+00	0,00E+00	-9,02E-03	0,00E+00	2,77E-01	-1,13E-04	-1,30E+00
theta1c	0,00E+00	0,00E+00	0,00E+00	0,00E+00	0,00E+00	0,00E+00	0,00E+00	0,00E+00	0,00E+00	-1,30E-03

Pilot to flap

(B.14)

References

[1] J. Mayo, The involuntary participation of a human pilot in a helicopter collective control loop, in: European Rotorcraft Forum, Amsterdam, Netherlands, 1989.

[2] T. Parham, D. Popelka, D. Miller, A. Froebel, V-22 pilot-in-the-loop aeroelastic stability analysis, in: AHS Forum Proceedings, Phoeniz, AZ, 1991.

[3] J. Venrooij, D. Yilmaz, M. Pavel, et al., Measuring biodynamic feedthrough in helicopters, in: European Rotorcraft Forum, Italy, 2011.

[4] Joost Venrooij, Measuring, modeling and mitigating biodynamic feedthrough, 2014.

[5] R.B. Walden, A retrospective survey of pilot–structural coupling instabilities in naval rotorcraft, in: AHS Forum Proceedings, 2007.

[6] M. Pavel, M. Jump, B. Dang-Vu, et al., Adverse rotorcraft pilot couplings — past, present and future challenges, Prog. Aerosp. Sci. 62 (2013) 1–51.

[7] P. Masarati, G. Quaranta, W. Basso, et al., Biodynamic tests for pilots' characterization on the BA–609 fly-by-wire tiltrotor, in: XX AIDAA Congress, Milano, Italy, 2009.

[8] R. Lantzsch, J. Wolfram, M. Hamers, Flight control and handling qualities evaluations considering air resonance, J. Am. Helicopter Soc. 59 (2014) 1–11.

[9] Anon, Aeronautical Design Standard. 33E-PRF, Performance Specification, Handling Qualities Requirements for Military Rotorcraft, US Army AMCOM, Redstone, Alabama, 2000.

[10] M. Gennaretti, M. Collela, J. Serafini, et al., Anatomy, modelling and prediction of aeroservoelastic rotorcraft–pilot-coupling, in: European Rotorcraft Forum, 2013.

[11] P. Masarati, G. Quaranta, Bioaeroservoelastic analysis of involuntary rotorcraft–pilot interaction, J. Comput. Nonlinear Dyn. 9 (3) (2014) 031009.

[12] V. Muscarello, G. Quaranta, P. Masarati, et al., Prediction and simulator verification of roll/lateral adverse aeroservoelastic rotorcraft–pilot couplings, J. Guid. Control Dyn. 39 (2016) 42–60.

[13] M. Pavel, G. Padfield, Understanding the peculiarities of rotorcraft–pilot-couplings, in: AHS Forum Proceedings, 2008.

[14] M. Pavel, Modeling lead-lag dynamics for rotorcraft–pilot-couplings investigation, in: AHS Forum Proceedings, Phoenix, AZ, 2010.

[15] T. Krysinski, F. Malburet, Mechanical Instability, Wiley-ISTE, 2011.

[16] R. Donham, S. Cardinale, I. Sachs, Ground and air resonance characteristics of a soft in-plane rigid-rotor system, J. Am. Helicopter Soc. 14 (4) (1969) 33–41.

[17] R. Bielawa, Rotary Wing Structural Dynamics and Aeroelasticity, AIAA Education Series, AIAA, 2006.

[18] J.B. Dryfoos, B.D. Kothmann, J. Mayo, An approach to reducing rotor–body coupled roll oscillations on the RAH-66 Comanche using modified roll rate feedback, in: AHS Forum Proceedings, Montreal, Canada, 1999.

[19] W. Johnson, Helicopter Theory, Dover Publications, Inc., 1980.

[20] B. Aponso, D. Johnston, W. Johnson, et al., Identification of higher order helicopter dynamics using linear modeling methods, J. Am. Helicopter Soc. 39 (3) (1994) 3–11.

[21] G. Tod, F. Malburet, J. Gomand, P.-J. Barre, B. Boudon, An energetic approach to aeroelastic rotorcraft–pilot couplings analysis, in: European Rotorcraft Forum, 2013.

[22] G. Tod, F. Malburet, J. Gomand, P.-J. Barre, An upper limb musculoskeletal model using bond graphs for rotorcraft–pilot couplings analysis, in: SIMBIO-M, Marseille, France, 2014.

[23] M. Lone, A. Cooke, Review of pilot models used in aircraft flight dynamics, Aerosp. Sci. Technol. 34 (2014) 55–74.

[24] R. Bielawa, Notes regarding fundamental understandings of rotorcraft aeroelastic instability, J. Am. Helicopter Soc. 32 (1987) 4–15.

[25] V. Muscarello, G. Quaranta, P. Masarati, The role of rotor coning in helicopter proneness to collective bounce, Aerosp. Sci. Technol. 36 (2014) 103–113.